



Short communication

Novel $\text{La}_2\text{NiO}_{4+\delta}$ and $\text{La}_4\text{Ni}_3\text{O}_{10-\delta}$ composites for solid oxide fuel cell cathodes

Russell J. Woolley, Stephen J. Skinner*

Department of Materials, Imperial College London, London SW7 2AZ, UK

HIGHLIGHTS

- Novel $\text{La}_2\text{NiO}_{4+\delta}$ and $\text{La}_4\text{Ni}_3\text{O}_{10-\delta}$ composites have been tested as IT-SOFC cathodes.
- These showed better performance than the single phases, particularly above 600 °C.
- This was due to the complimentary nature of the conductivities of the two phases.
- The performance of these composites represents best-in-class for these materials.

ARTICLE INFO

Article history:

Received 19 March 2013

Received in revised form

2 June 2013

Accepted 18 June 2013

Available online 27 June 2013

Keywords:

Lanthanum nickelate

Ruddlesden Popper

Composite

Solid oxide fuel cell

Cathode

ABSTRACT

Ruddlesden–Popper phases of the formula $(\text{LaNiO}_3)_n\text{LaO}$ are potential materials for intermediate-temperature solid oxide fuel cell cathodes. The $n = 1$ phase $\text{La}_2\text{NiO}_{4+\delta}$ is known to have good ionic conductivity but its performance as a single-phase cathode is limited by its electronic conductivity. The $n = 3$ phase $\text{La}_4\text{Ni}_3\text{O}_{10-\delta}$ is known to have good total conductivity but has been little-explored as a cathode. In this study we explore composite electrodes of these two materials with a view to taking advantage of their complimentary properties. The performance of these electrodes is compared to that of the single-phase end-members and is found to be improved above 600 °C. A 50:50 wt.% $\text{La}_2\text{NiO}_{4+\delta}:\text{La}_4\text{Ni}_3\text{O}_{10-\delta}$ mix gave the best performance and represents best-in-class for these materials.

© 2013 Elsevier B.V. All rights reserved.

1. Introduction

Traditionally solid oxide fuel cell (SOFC) cathode materials have been selected from oxides with the three-dimensionally isotropic perovskite structure; however there is a growing consensus that such materials are reaching the limits of their performance. Hence increasing efforts are being made to study other structure types [1], particularly layered materials [2]. Layered Ruddlesden–Popper (R–P) phases have recently been studied for potential application as SOFC cathodes. These have the generic formula $(\text{ABO}_3)_n\text{AO}$ and consist of perovskite-like ABO_3 slabs n layers thick separated by a single rock salt-like AO layer (Fig. 1). In particular the $(\text{LaNiO}_3)_n\text{LaO}$ series has been considered. For this series $n = \infty$ is the perovskite LaNiO_3 . Phases with $n = 1, 2$, and 3 correspond to

$\text{La}_2\text{NiO}_{4+\delta}$, $\text{La}_3\text{Ni}_2\text{O}_{7-\delta}$, $\text{La}_4\text{Ni}_3\text{O}_{10-\delta}$ respectively. Hereafter these are abbreviated as L2N1, L3N2 and L4N3. The bulk of the literature focusses on L2N1 and this stems from the mixed ionic–electronic conductivity observed in this phase at temperatures appropriate for intermediate-temperature (IT) SOFCs, 500–700 °C [3,4]. It is known that L2N1 has interstitial oxygen content which resides in the LaO layers [5,6]. This is responsible for the strong anisotropic ionic conductivity (σ_i) observed [7–9]. However, L2N1 has insufficient total conductivity (σ_{tot}) for IT-SOFC cathode purposes, so recently the higher-order phases L3N2 and L4N3 have been studied [10–12]. σ_{tot} is reported to increase with n —this being the thickness of the perovskite slabs in the layered structure—with L4N3 showing metallic conductivity [12]. Some studies have demonstrated improved performance of L4N3 over L2N1 [10,12] presumably due to this improved total conductivity. σ_i for L4N3 has yet to be fully explored due to the inability to produce a sample of sufficient density [10], but if present is expected to occur via oxygen vacancy migration [13].

* Corresponding author. Tel.: +44 (0)20 7594 6782.

E-mail address: s.skinner@imperial.ac.uk (S.J. Skinner).

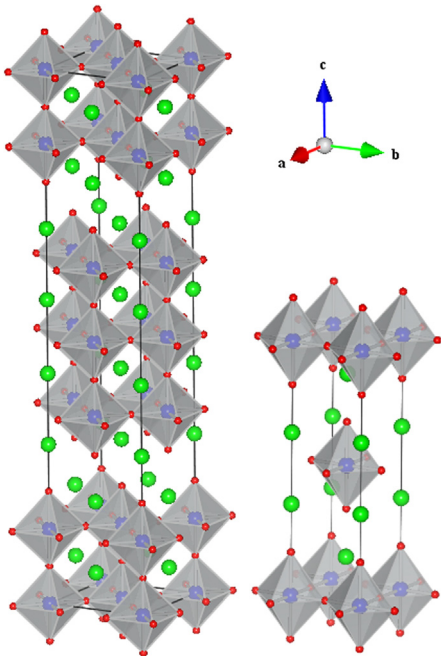


Fig. 1. $n = 1$ (right) and $n = 3$ (left) Ruddlesden–Popper structure adopted by $\text{La}_2\text{NiO}_{4+\delta}$ and $\text{La}_4\text{Ni}_3\text{O}_{10-\delta}$ respectively. La = green; Ni = blue; O = red. (For interpretation of the references to colour in this figure legend, the reader is referred to the web version of this article.)

It is known that composite cathode materials can show improved performance over single phases. This is typically achieved by combining the good σ_i of an electrolyte material with the good σ_{tot} of a perovskite oxide. Ancillary benefits include a better thermal expansion coefficient (TEC) match between cathode and electrolyte. This is exemplified by the high performance observed in $\text{Ce}_{0.9}\text{Gd}_{0.1}\text{O}_{2-\delta}$ (CGO10) and $\text{La}_{0.6}\text{Sr}_{0.4}\text{Co}_{0.2}\text{Fe}_{0.8}\text{O}_{3-\delta}$ (LSCF) composite cathodes [14,15]. L2N1 has been utilised as part of a composite with LSCF and resulted in an improved TEC [16], aside from this little work has been carried out on composites using layered phases. Within the La–Sr–Co–O system it has been shown that oxygen surface exchange kinetics can be enhanced by introducing heterointerfaces between perovskite and $n = 1$ phases, $(\text{La},\text{Sr})\text{CoO}_3$ and $(\text{La},\text{Sr})_2\text{CoO}_4$ [17,18], and even cobalt oxides [19]. These reports indicate the potential of multiphasic electrodes containing layered oxides.

Considering the properties of L2N1 and L4N3 it becomes apparent that they are good candidates to form a composite electrode, the former with good σ_i and the latter with good σ_{tot} . To further explore these promising materials we present electrochemical data on novel composite electrodes of L2N1 and L4N3 compared to single-phase electrodes of the end-member materials.

2. Materials and methods

2.1. Symmetrical cell fabrication

Pellets of $\text{La}_{0.8}\text{Sr}_{0.2}\text{Ga}_{0.8}\text{Mg}_{0.2}\text{O}_{3-\delta}$ (LSGM8282, hereafter abbreviated as LSGM) (Praxair) were uniaxially then isostatically pressed and sintered at 1450 °C for 8 h. Archimedes testing confirmed their density at >95% theoretical. Electrode inks were manufactured by first ball-milling electrode powders in ethanol for 24 h then three-roll milling with a commercial ink vehicle (Fuel Cell Materials 311006). L2N1 was obtained from a commercial source (CerPoTech,

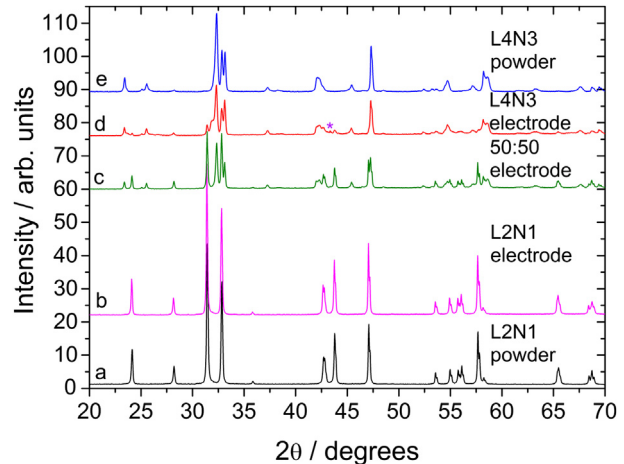


Fig. 2. XRD patterns of (a) $\text{La}_2\text{NiO}_{4+\delta}$ and (e) $\text{La}_4\text{Ni}_3\text{O}_{10-\delta}$ powders compared with as-sintered symmetrical cell electrodes of (b) $\text{La}_2\text{NiO}_{4+\delta}$, (d) $\text{La}_4\text{Ni}_3\text{O}_{10-\delta}$, and (c) 50:50. Extra peaks for the $\text{La}_4\text{Ni}_3\text{O}_{10-\delta}$ electrode correspond to reactivity towards lower-order phases and NiO (marked); no reactivity observed on sintering composite electrodes or $\text{La}_2\text{NiO}_{4+\delta}$.

synthesised by a spray pyrolysis technique) and L4N3 synthesised by a sol–gel method; solutions of known concentrations of $\text{La}(\text{N}-\text{O}_3)_3 \cdot 6\text{H}_2\text{O}$ and $\text{Ni}(\text{NO}_3)_2 \cdot 6\text{H}_2\text{O}$ were stirred with calculated excesses of citric acid and ethylene glycol. Water was evaporated on a hotplate and the resulting gel decomposed at 300 °C for 12 h then 600 °C for 12 h. The resulting powder was ground and sintered at 1050 °C for 48 h. Identity and phase purity for both phases were confirmed by powder X-ray diffraction (XRD) (Fig. 2a and e). Inks were deposited by brush-coating onto the electrolyte pellets then sintering at 1000 °C for 4 h, except in the case of the 100% L4N3 ink which was sintered at 1200 °C for 4 h. Electrode adherence was checked by the Scotch tape test, a simple and reliable method [20]. The finished cells, detailed in Table 1, had electrodes approx. 30 μm thick with overall dimensions 11 mm Ø × 1.5 mm.

2.2. Total conductivity of electrode layers

The van der Pauw technique can be used to measure the lateral conductivity of a flat sample of any shape [21,22]. 5 × 5 mm square layers of the prepared inks were screen-printed onto dense LSGM pellets and sintered using the same regime as the symmetrical cells. These squares were mounted in a spring-loaded holder as described by Esquirol [23]; small electrical contacts are made at each corner. Defining these as 1, 2, 3 and 4 we can obtain two characteristic resistances R_A and R_B (Fig. 3). Van der Pauw has shown that;

$$\exp\left(\frac{-\pi d R_A}{\rho}\right) + \exp\left(\frac{-\pi d R_B}{\rho}\right) = 1$$

Table 1

Electrode details and nomenclature for symmetrical cells tested. Adherence between electrode and LSGM electrolyte was confirmed by the Scotch tape test.

Electrode composition	Sintering regime	Nomenclature
100% $\text{La}_2\text{NiO}_{4+\delta}$	1000 °C × 4 h	L2N1
60 wt.% $\text{La}_2\text{NiO}_{4+\delta}$ + 40 wt.% $\text{La}_4\text{Ni}_3\text{O}_{10-\delta}$	1000 °C × 4 h	60:40
50 wt.% $\text{La}_2\text{NiO}_{4+\delta}$ + 50 wt.% $\text{La}_4\text{Ni}_3\text{O}_{10-\delta}$	1000 °C × 4 h	50:50
40 wt.% $\text{La}_2\text{NiO}_{4+\delta}$ + 60 wt.% $\text{La}_4\text{Ni}_3\text{O}_{10-\delta}$	1000 °C × 4 h	40:60
100% $\text{La}_4\text{Ni}_3\text{O}_{10-\delta}$	1200 °C × 4 h	L4N3

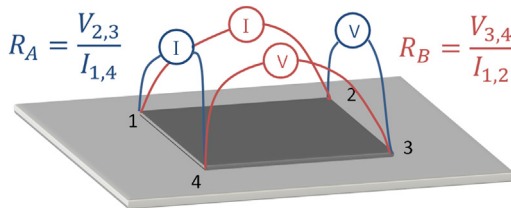


Fig. 3. Electrical contacts that define two characteristic resistances for total conductivity tests. Dark grey: screen-printed electrode; light grey: LSGM substrate.

where the sample has a thickness d , found by post-test SEM analysis; and conductivity ρ , found by solving numerically using a least-squares method. The conductivity of LSGM over the tested temperature range, 400–700 °C, is of the order of 10^{-2} S cm $^{-1}$ [24]. The conductivity of the screen-printed L2N1/L4N3 layers will dominate this therefore any contribution from the LSGM pellet is assumed to be negligible.

2.3. Other techniques

AC Impedance spectroscopy (ACIS) was carried out using a Solartron 1260a impedance/gain-phase analyser with a thermocouple positioned close to the tested cell to accurately record the temperature; scanning electron microscopy (SEM) images were obtained using a JEOL 5610 LV; XRD patterns were collected using a PANalytical X'Pert Pro MPD using Ni filtered Cu K α radiation with tube voltage/current at 40 kV/40 mA.

3. Results and discussion

3.1. Characterisation of as-sintered electrodes

3.1.1. Electrode adherence

After sintering the symmetrical cells the Scotch tape test was carried out to check the electrode was adequately adhered to the electrolyte. A regime of 1000 °C for 4 h gave good adherence for the L2N1 and composite electrodes; to achieve this for L4N3 electrodes it was necessary to sinter at 1200 °C for 4 h.

3.1.2. Phase changes during sintering

Fig. 2 presents XRD patterns collected for the electrodes after sintering. For L4N3 extra peaks are present in the electrode pattern (Fig. 2d) over the powder pattern (Fig. 2e). These peaks can be assigned to the formation during the sintering process of lower-order R–P phases and nickel oxide. This behaviour can be explained using the La–Ni–O phase diagram proposed by Zinkevich and Aldinger [25] shown in Fig. 4. Heating L4N3 to 1200 °C takes it into a region of L3N2 + NiO and very close to a region of L2N1 + NiO, agreeing well with what is seen in the diffraction pattern.

No reactivity was observed on sintering for the single phase L2N1 or L2N1:L4N3 composite electrodes. The diffraction patterns for the latter are a linear combination of the powder patterns for the two materials (Fig. 2a, c, e). Across the range of the compositions, 60:40–50:50–40:60, XRD patterns show the expected concurrent drop in intensity of L2N1 peaks and increase in L4N3 peaks. This is easily seen in the first two peaks—the (111) reflections for each phase (Fig. 5). The integrated intensities of these peaks are as expected across the changing L2N1:L4N3 ratio (Table 2). The phase diagram in Fig. 4 has no two-phase L2N1–L4N3 region and predicts that L3N2 would form from a mix of the two at 1000 °C. This was not observed in this work, which indicates that the sintering time and interface between the phases was not sufficient to result in reactivity within the detection limit of XRD.

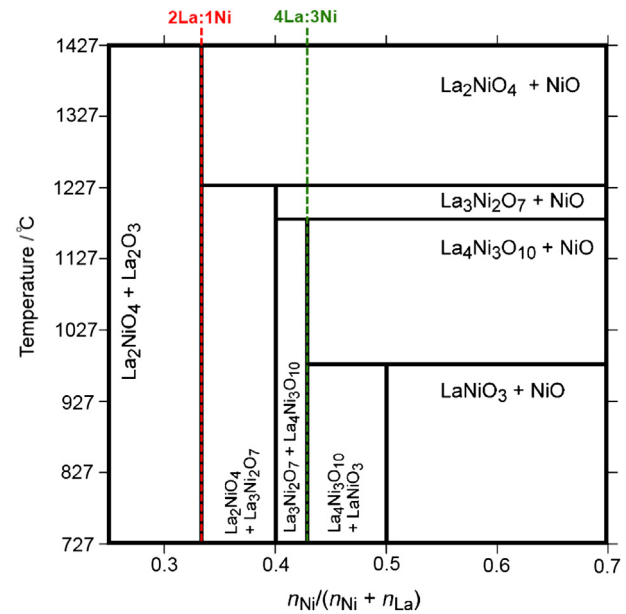


Fig. 4. La–Ni–O phase diagram adapted from Zinkevich and Aldinger [25]. Marked are lines corresponding to a 2:1 and 4:3 La:Ni ratio.

3.1.3. Total conductivity of electrode layers

The temperature dependence of σ_{tot} for the R–P electrodes tested is displayed in Fig. 6. The $n = 3$ phase L4N3 has higher conductivity than the $n = 1$ phase L2N1; it is well-established that σ_{tot} in $(\text{LaNiO}_3)_n\text{LaO}$ increases with n [10,12]. Values for L4N3 were 20 S cm $^{-1}$ at 400 °C increasing to 30 S cm $^{-1}$ at 700 °C. Over the temperature range σ_{tot} for each electrode follows the same trend; it is relatively constant up to 550 °C followed by an increase over the remainder. Comparisons are drawn with Amow et al. [10] who observed a decrease in σ_{tot} in L2N1 and L4N3 between 400 and 700 °C and greater overall conductivities than reported here. A key difference is that Amow tested bars sintered to maximise the materials density. In this study we tested porous layers and as such believe these data to be more relevant to potential applications of these materials as SOFC cathodes. It is not surprising that σ_{tot} for a porous layer is lower than that for a dense bar, however the change in trend over the temperature range was not anticipated. These variations highlight the importance of processing and microstructure in testing SOFC materials.

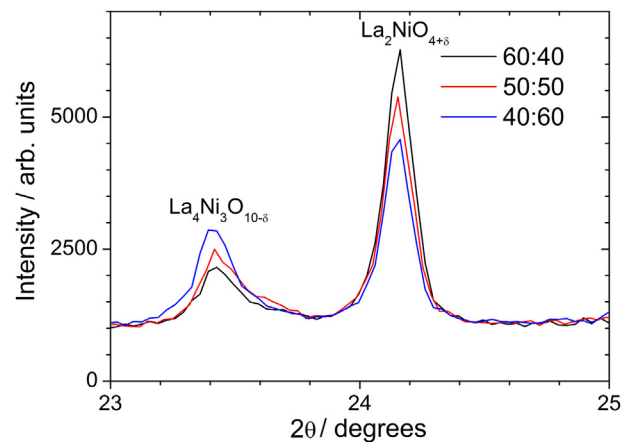


Fig. 5. (111) Reflections for $\text{La}_4\text{Ni}_3\text{O}_{10-\delta}$ (23.4°) and $\text{La}_2\text{NiO}_{4+\delta}$ (24.2°) in as-sintered 60:40, 50:50 and 40:60 $\text{La}_2\text{NiO}_{4+\delta}:\text{La}_4\text{Ni}_3\text{O}_{10-\delta}$ symmetrical cells. Relative intensity shifts are as expected due to the changing $\text{La}_2\text{NiO}_{4+\delta}:\text{La}_4\text{Ni}_3\text{O}_{10-\delta}$ ratio (cf. Table 2).

Table 2

Integrated peak intensities for $\text{La}_2\text{NiO}_{4+\delta}$ (24.2°) and $\text{La}_4\text{Ni}_3\text{O}_{10-\delta}$ (23.4°) (111) peaks in Fig. 5. The relative intensities of the peaks are as expected given the changing L2N1:L4N3 ratio in the electrodes.

L2N1:L4N3 ratio	L2N1 (111) peak intensity arb. units	L4N3 (111) peak intensity arb. units	Intensity ratio normalised to 50:50 ratio	Expected ratio
60:40	833	275	1.54	1.50
50:50	731	371	1.0	1.0
40:60	608	469	0.66	0.67

3.2. Electrochemical testing

To determine the suitability of these materials with regard to IT-SOFC cathode use, ACIS measurements were carried out on symmetrical cells from 507 to 710°C . A typical Nyquist plot at approx. 600°C is shown in Fig. 7 and normalised area-specific resistance (ASR) values for each electrode over the temperature range are displayed in Fig. 8. Data were fitted using a typical equivalent-circuit model with two R/CPE (constant phase element) components as shown in Fig. 7. The CPE exponents show significant deviations from unity meaning that equivalent capacitance values calculated for the CPEs will have little physical meaning.

The composite electrodes had an activation energy of around 0.6 eV over the whole temperature range. L4N3 shares this value but with much higher ASR values. L2N1 shows a change in gradient from around 0.6 eV from 500 to 600°C to 0.5 eV from 600 to 700°C . In the lower-temperature region the performance of L2N1 was comparable to the composites but above 600°C it was inferior. The change in activation energy in L2N1 indicates a change in the electrode-limiting step. Similar behaviour has been observed before [13] but is not present in all cases. The activation energy values found in this study are in a similar region to those found by Aguadero et al. for L2N1 on LSGM [26], but again differ from other cases. These variations further emphasise the importance of processing and microstructure on the properties of SOFC electrodes. What is clear from this work is that above 600°C a L2N1:L4N3 composite provides a better electrode than either of the single phases.

Comparisons are drawn between the ASR data in Fig. 8 and the total conductivity data in Fig. 6. Below 600°C σ_{tot} for the composites is similar to that of L2N1; above 600°C σ_{tot} for the composites increases faster than for L2N1, and tends towards that of L4N3. This coincides with the region of improved performance of the composites over L2N1. Here the advantage of the composite is

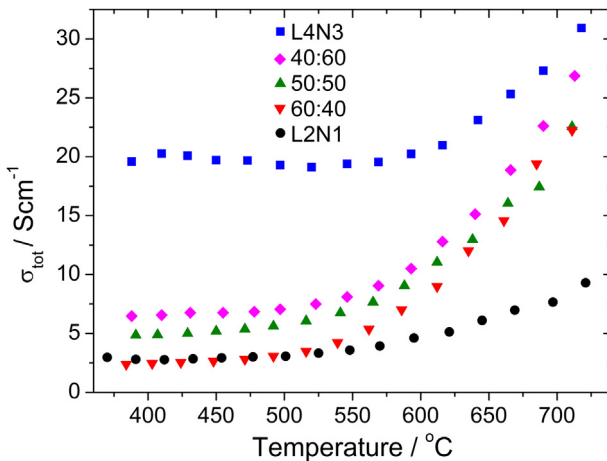


Fig. 6. Total conductivity as a function of temperature for tested R-P materials (cf. Fig. 3).

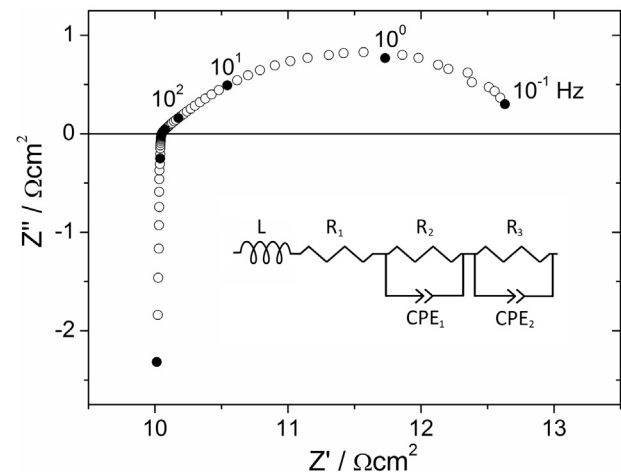


Fig. 7. Typical Nyquist plot for composite symmetrical cell at approx. 600°C (in this case 50:50 at 606°C) and equivalent-circuit model used to fit data.

highlighted. We believe that the good σ_i of L2N1 is maintained over the whole temperature range, and that the addition of L4N3 enhances σ_{tot} acting to improve the performance above 600°C .

From the different ratios explored a 50:50 wt.% composite gave the best results with ASRs at 500, 550, 600, 650, and 700°C calculated to be 38.1, 10.3, 3.45, 1.37 and $0.62 \Omega \text{ cm}^2$ respectively. This compares favourably with literature data and is believed to be the best performance for electrodes of this class. These ASR values are lower than that quoted for L2N1 [27,28]; a copper-doped phase $\text{La}_2\text{Ni}_{0.6}\text{Cu}_{0.4}\text{O}_{4+\delta}$ [26]; L3N2 [11]; and the various La–Ni electrodes discussed in a recent review [2].

3.3. Post-test microstructural analysis

Fig. 9 shows SEM images of symmetrical cells obtained after ACIS testing. It is to be noted that by this method one cannot distinguish between the L2N1 and L4N3 constituting the composites. This is as expected given the nature of the physical processes occurring during image acquisition. From these images it can be seen that a further reason for the performance enhancement of the composite electrodes over single phases is their improved microstructure. The L4N3 electrode (Fig. 9a) lacks interconnectivity and has a broad distribution of particle sizes with series of voids

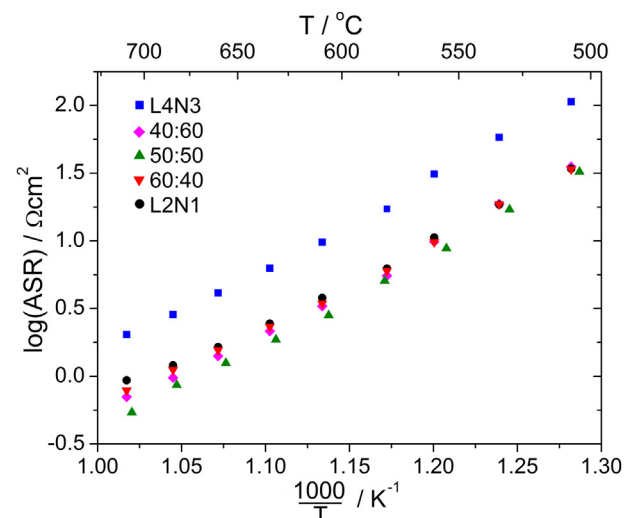


Fig. 8. Log (ASR) vs $1000/T$ for the symmetrical cells tested.

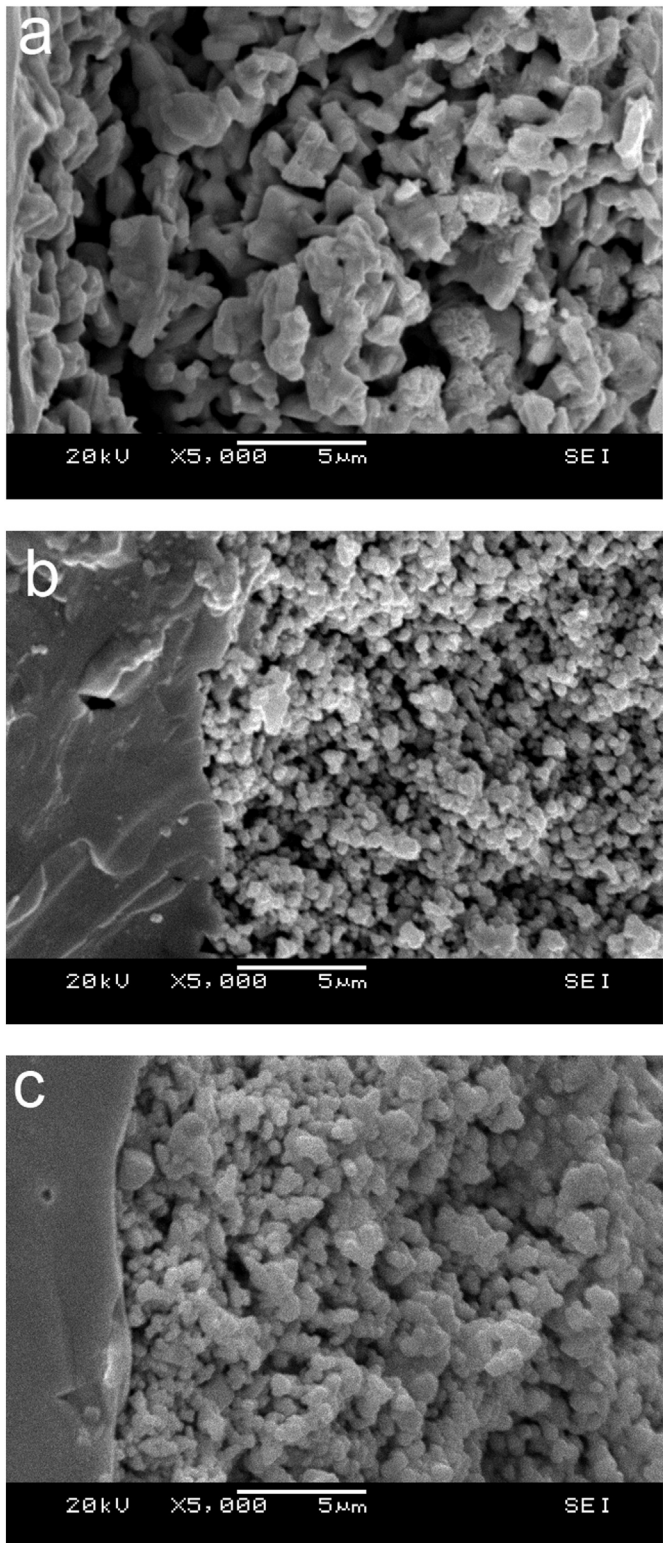


Fig. 9. SEM images of symmetrical cells after testing. (a) $\text{La}_4\text{Ni}_3\text{O}_{10-\delta}$; (b) $\text{La}_2\text{NiO}_{4+\delta}$; (c) 50:50.

throughout. This is consistent with the reported difficulty in sintering this phase [10]. The L2N1 electrode (Fig. 9b) displays a relatively uniform particle size distribution but poor interconnectivity and adherence to the electrolyte. The composite cells, exemplified here by 50:50 (Fig. 9c), show on balance the best microstructure. They are well-adhered to the electrolyte and

display good interconnectivity meaning that a greater number of conductive pathways will be present. The microstructure is still not ideal however; the particle size distribution could be improved upon. This is reflected in the markedly depressed nature of the arcs in the Nyquist plots (Fig. 7). With optimisation of ink constitution and deposition method it is hoped that the microstructure and therefore performance of these electrodes could be further improved.

3.4. Further comments

We acknowledge that the ASR values reported here are higher than the $0.15 \Omega \text{ cm}^2$ target suggested by Steele [29]. This target has already been met in the intermediate-temperature range by a variety of perovskite cathodes. These materials typically have a large concentration of oxygen vacancies. This is achieved by partial substitution of a trivalent rare-earth ion by divalent strontium, exemplified by the much-studied LSCF family [14,15]. However, the presence of strontium leads to problematic issues of degrading long-term performance. For IT-SOFCs to breakthrough into the commercial market they require sufficient stability; they must resist materials degradation whilst remaining at operating temperature for long periods of time, ideally many years. Under operating conditions strontium is known to segregate to the surface of perovskite cathodes leading to the formation of an insulating layer [30]. A further degradation issue is chromium poisoning from steel interconnects. This has been shown to occur in the Sr-free perovskite $\text{LaNi}_{0.6}\text{Fe}_{0.4}\text{O}_3$ [31], but is also known to be exacerbated by strontium, which acts as a nucleating agent for the formation of Cr-containing species [32]. These degradation phenomena have been barriers to the commercialisation of IT-SOFCs based on Sr-doped perovskite cathodes. Hence, one of the reasons behind choosing the $(\text{LaNiO}_3)_n\text{LaO}$ phases used in this study is that they do not require strontium doping for the presence of significant concentrations of ionic charge carriers—oxygen interstitial ions or oxygen vacancies. Detailed investigations into their long-term stability have yet to be carried out, however the high Ni^{3+} content of L4N3 is believed to result in its inherent stability in the intermediate-temperature range [10]. Furthermore, it is believed that cathode materials free of strontium would be more tolerant towards Cr poisoning [33]. Hence, it is expected that these La–Ni R–P materials will show better stability as IT-SOFC cathodes than Sr-doped perovskites. This gives further reason for continued research in this area.

4. Conclusion

L2N1, L4N3, and novel L2N1:L4N3 composites have been tested as potential IT-SOFC cathodes. On sintering symmetrical cells reactivity was observed in the single-phase L4N3 electrode. This is explained via the relevant thermodynamic literature. The formation of a composite leads to improved performance over the single phases, particularly above 600°C . This is assigned to the combination of good σ_i and σ_{tot} from the two components of the composite, as well as an improved microstructure. A 50:50 wt.% mix gave the best results with an ASR at 700°C of $0.62 \Omega \text{ cm}^2$. This represents best-in-class for these La–Ni R–P phases. With further microstructural optimisation it is expected that the performance of these can be improved upon and hence these novel composites represent promising candidates for further study.

Acknowledgements

The authors gratefully acknowledge the EPSRC for funding under the SUPERGEN Fuel Cells programme. We would also like to

thank Kuan-Ting Wu and Toby Basey-Fisher for their assistance with the total conductivity data.

References

- [1] A. Aguadero, L. Fawcett, S. Taub, R.J. Woolley, K.-T. Wu, N. Xu, J. Kilner, S. Skinner, *Journal of Materials Science* 47 (2012) 3925–3948.
- [2] A. Tarancón, M. Burriel, J. Santiso, S.J. Skinner, J.A. Kilner, *Journal of Materials Chemistry* 20 (2010) 3799–3813.
- [3] V.V. Kharton, A.P. Viskup, E.N. Naumovich, F.M.B. Marques, *Journal of Materials Chemistry* 9 (1999) 2623–2629.
- [4] S.J. Skinner, J.A. Kilner, *Solid State Ionics* 135 (2000) 709–712.
- [5] M.S.D. Read, M.S. Islam, F. King, F.E. Hancock, *The Journal of Physical Chemistry B* 103 (1999) 1558–1562.
- [6] W. Paulus, A. Cousson, G. Dhalenne, J. Berthon, A. Revcolevschi, S. Hosoya, W. Treutmann, G. Heger, R. Le Toquin, *Solid State Sciences* 4 (2002) 565–573.
- [7] L. Minervini, R.W. Grimes, J.A. Kilner, K.E. Sickafus, *Journal of Materials Chemistry* 10 (2000) 2349–2354.
- [8] J. Bassat, P. Odier, A. Villesuzanne, C. Marin, M. Pouchard, *Solid State Ionics* 167 (2004) 341–347.
- [9] A. Chroneos, D. Parfitt, J.A. Kilner, R.W. Grimes, *Journal of Materials Chemistry* 20 (2010) 266.
- [10] G. Amow, I. Davidson, S. Skinner, *Solid State Ionics* 177 (2006) 1205–1210.
- [11] Z. Lou, J. Peng, N. Dai, J. Qiao, Y. Yan, Z. Wang, J. Wang, K. Sun, *Electrochemistry Communications* 22 (2012) 97–100.
- [12] S. Takahashi, S. Nishimoto, M. Matsuda, M. Miyake, *Journal of the American Ceramic Society* 93 (2010) 2329–2333.
- [13] G. Amow, S.J. Skinner, *Journal of Solid State Electrochemistry* 10 (2006) 538–546.
- [14] W.G. Wang, M. Mogensen, *Solid State Ionics* 176 (2005) 457–462.
- [15] V. Dusastre, J.A. Kilner, *Solid State Ionics* 126 (1999) 163–174.
- [16] M. Chen, B.H. Moon, S.H. Kim, B.H. Kim, Q. Xu, B.G. Ahn, *Fuel Cells* 12 (2012) 86–96.
- [17] T. Kawada, M. Sase, M. Kudo, K. Yashiro, K. Sato, J. Mizusaki, N. Sakai, T. Horita, K. Yamaji, H. Yokokawa, *Solid State Ionics* 177 (2006) 3081–3086.
- [18] M. Sase, F. Hermes, K. Yashiro, K. Sato, J. Mizusaki, T. Kawada, N. Sakai, H. Yokokawa, *Journal of the Electrochemical Society* 155 (2008) B793–B797.
- [19] J. Hayd, H. Yokokawa, E. Ivers-Tiffée, *Journal of the Electrochemical Society* 160 (2013) F351–F359.
- [20] H. Nguyen, *Microwave and Optical Technology Letters* 16 (1997) 66–72.
- [21] L.J. van der Pauw, *Philips Technical Review* 20 (1958) 220–224.
- [22] L.J. van der Pauw, *Philips Research Reports* 13 (1958) 1–9.
- [23] A. Esquirol, N.P. Brandon, J.A. Kilner, M. Mogensen, *Journal of the Electrochemical Society* 151 (2004) A1847–A1855.
- [24] K. Huang, R.S. Tichy, J.B. Goodenough, *Journal of the American Ceramic Society* 81 (1998) 2565–2575.
- [25] M. Zinkevich, F. Aldinger, *Journal of Alloys and Compounds* 375 (2004) 147–161.
- [26] A. Aguadero, J.A. Alonso, M.J. Escudero, L. Daza, *Solid State Ionics* 179 (2008) 393–400.
- [27] K. Zhao, Q. Xu, D.-P. Huang, W. Chen, M. Chen, B.-H. Kim, *Journal of Solid State Electrochemistry* 16 (2012) 9–16.
- [28] K. Zhao, Q. Xu, D.-P. Huang, M. Chen, B.-H. Kim, *Ionics* 18 (2012) 75–83.
- [29] B. Steele, *Solid State Ionics* 86–88 (1996) 1223–1234.
- [30] D. Oh, D. Gostovic, E. Wachsmann, *Journal of Materials Research* 27 (2012) 1992–1999.
- [31] M.K. Stodolny, B.A. Boukamp, D.H.A. Blank, F.P.F. van Berkel, *Journal of Power Sources* 209 (2012) 120–129.
- [32] X. Chen, L. Zhang, S.P. Jiang, *Journal of the Electrochemical Society* 155 (2008) B1093–B1101.
- [33] C. Sun, R. Hui, J. Roller, *Journal of Solid State Electrochemistry* 14 (2010) 1125–1144.